J. Fluid Mech. (2012), *vol.* 691, *pp.* 568–582. © Cambridge University Press 2012
doi:10.1017/jfm.2011.493

Heat transfer by rapidly rotating Rayleigh–Bénard convection

E. M. King[1]†, **S. Stellmach**[2] **and J. M. Aurnou**[3]

[1] Department of Earth and Planetary Science, University of California, Berkeley, CA 94720-4767, USA
[2] Institut für Geophysik, Westfälische Wilhelms-Universität Münster, Arbeitsgruppe Geodynamik, Corrensstraße 24, 48149 Münster, Germany
[3] Department of Earth and Space Sciences, University of California, Los Angeles, CA 90095-1567, USA

(Received 2 February 2011; revised 2 November 2011; accepted 5 November 2011)

Turbulent, rapidly rotating convection has been of interest for decades, yet there exists no generally accepted scaling law for heat transfer behaviour in this system. Here, we develop an exact scaling law for heat transfer by geostrophic convection, $Nu = (Ra/Ra_c)^3 = 0.0023\, Ra^3 E^4$, by considering the stability of the thermal boundary layers, where Nu, Ra and E are the Nusselt, Rayleigh and Ekman numbers, respectively, and Ra_c is the critical Rayleigh number for the onset of convection. Furthermore, we use the scaling behaviour of the thermal and Ekman boundary layer thicknesses to quantify the necessary conditions for geostrophic convection: $Ra \lesssim E^{-3/2}$. Interestingly, the predictions of both heat flux and regime transition do not depend on the total height of the fluid layer. We test these scaling arguments with data from laboratory and numerical experiments. Adequate agreement is found between theory and experiment, although there is a paucity of convection data for low $Ra\, E^{3/2}$.

Key words: Bénard convection, geostrophic turbulence, rotating flows

1. Theory

1.1. *Introduction*

Rayleigh–Bénard convection (RBC) is a classical system used to examine turbulence. RBC consists of a horizontal fluid layer of infinite extent that is destabilized by an imposed adverse temperature gradient. The system's dynamics are determined by the Rayleigh and Prandtl numbers, Ra and Pr (see table 1 for definitions), which characterize the strength of thermal forcing and fluid properties, respectively. Aside from permitting the investigation of fundamental turbulent fluid dynamics, this system also represents a simplified analogue for many geophysical and astrophysical environments. Planetary and stellar convection systems, though, are subject to Coriolis forces resulting from the intrinsic rotation of their host bodies. This additional influence introduces a third parameter, a non-dimensional rotation period called the Ekman number, E. In order to examine the influence of rotation on

---

† Email address for correspondence: ericmking@gmail.com

Parameter	Laboratory	Simulations
$Ra \equiv \alpha_T g \Delta T h^3/(\nu\kappa)$	$10^6 \lesssim Ra \lesssim 10^{10}$	$10^3 \lesssim Ra \lesssim 10^9$
$E \equiv \nu/(2\varOmega h^2)$	$3\times 10^{-6} \lesssim E \lesssim \infty$	$10^{-6} \leqslant E \leqslant \infty$
$Pr \equiv \nu/\kappa$	$4.5 \lesssim Pr \lesssim 11$	$1 \leqslant Pr \leqslant 100$
$Nu \equiv qh/(k\Delta T)$	$3 \lesssim Nu \lesssim 110$	$1 \lesssim Nu \lesssim 50$

TABLE 1. Relevant non-dimensional parameters, and parameter ranges from laboratory experiments and numerical simulations. Dimensional quantities are as follows: α_T is the fluid's coefficient of thermal expansivity; g is gravitational acceleration; ΔT is the temperature drop across the fluid layer; h is the depth of the fluid layer; ν is viscous diffusivity; κ is thermal diffusivity; $\varOmega$ is the angular rotation rate; q is mean heat flux; and k is thermal conductivity.

convection dynamics, we investigate the Rayleigh–Bénard configuration rotating about a vertical axis.

1.2. *Non-rotating convection*

We begin our investigation of rotating convection with a brief overview of heat transport by non-rotating RBC. Accurate descriptions of the Nusselt number, Nu, which characterizes the efficiency of convective heat transfer, have been of interest to the turbulence community for decades, and scalings of the type $Nu \propto Ra^{\alpha}$ have typically been sought both theoretically and experimentally (e.g. Ahlers, Grossmann & Lohse 2009). A scaling exponent of $\alpha = 1/3$ was first developed by the marginal stability boundary analysis of Malkus (1954).

This classical 1/3 scaling law can be developed through consideration of boundary layer stability as follows. In an infinite half-space, bounded and heated from below at rate q, a quiescent fluid will become unstable above some height δ when a locally defined Rayleigh number $Ra_\delta = \alpha_T g \Delta T_\delta \delta^3/(\nu\kappa)$ is larger than the critical value, $Ra_c = constant$ (Pellew & Southwell 1940). Here, ΔT_δ is the temperature drop across this marginally stable boundary layer. Thus, instability should occur when

$$\delta^3 \Delta T_\delta \approx Ra_c \frac{\nu\kappa}{\alpha_T g}. \tag{1.1}$$

Instead of an infinite half-space, let us consider a layer of finite depth h with marginally stable thermal boundary layers adjacent to each boundary. We make the following two assumptions to relate this local stability criterion to total heat transport. Let us first assume that the temperature drop across the layer occurs mostly in the boundary layers, $\Delta T \approx 2\Delta T_\delta$. This permits us to rewrite (1.1) as

$$\delta/h \approx (Ra/Ra_c)^{-1/3}. \tag{1.2}$$

Let us also assume that heat is transferred primarily by conduction within the stable boundary layer, $\Delta T_\delta \approx q\delta/k$. The stability criterion therefore becomes

$$Nu \approx h/\delta \approx (Ra/Ra_c)^{1/3}. \tag{1.3}$$

Experimental studies have not been able to verify this classical theoretical scaling unequivocally. At moderately high Rayleigh numbers ($10^4 \lesssim Ra \lesssim 10^{10}$), and moderate Prandtl numbers ($Pr = O(1)$), experimental studies typically find scaling exponents nearer to $\alpha = 2/7$ (e.g. Castaing *et al.* 1989; Chilla *et al.* 1993; Glazier *et al.* 1999).

As the Rayleigh number increases further, however, simulations and experiments produce scaling exponents that approach $\alpha = 1/3$ (e.g. Amati *et al.* 2005; Niemela & Sreenivasan 2006) – barring any possible transitions to the so-called ultimate regime Ahlers *et al.* (2009). Furthermore, some measurements of thermal boundary layer thicknesses themselves in experiments and simulations have been found to follow a $Ra^{-1/3}$ scaling (e.g. Sun, Cheung & Xia 2008; this work). This indicates that, although the heat transfer scaling law (1.3) has not been verified exactly, the underlying mechanism of boundary layer instability (1.2) may apply.

1.3. *Rotating convection*

Flows in the presence of strong rotation are often typified by a first-order force balance between the Coriolis force and pressure gradient, which is known as the geostrophic balance. The Coriolis force has a stabilizing effect on convection, such that the onset of convection occurs at higher Ra for decreasing E. Chandrasekhar (1953) predicted that the critical Rayleigh number for instability scales as $Ra_c \propto E^{-4/3}$ for rapidly rotating convection ($E \lesssim 10^{-4}$). Thus, for small E, the critical Rayleigh number can be orders of magnitude larger than that for non-rotating fluids. This illustrates how the role of diffusive stabilization is secondary to that by rotation as $E \to 0$.

As was done above for non-rotating convection, so can we develop a heat transfer scaling law based on boundary layer stability for rapidly rotating flows as follows. Consider again an infinite half-space bounded and heated from below at a flux rate q, but this time also rotating at rate $\varOmega$. Above height δ, the quiescent (in the rotating reference frame) fluid becomes buoyantly unstable due to the adverse temperature gradient. Assuming that the stabilizing effect of the Coriolis force dominates that of diffusion, the local stability criterion is $Ra_\delta / Ra_c^\delta > 1$, where $Ra_c^\delta = A E_\delta^{-4/3}$, A is a constant and $E_\delta = \nu/(2\varOmega\delta^2)$. We can write this boundary layer stability criterion in terms of the boundary layer thickness and temperature drop as

$$\delta^{1/3} \Delta T_\delta \approx A \frac{\nu\kappa}{\alpha_T g} \left(\frac{2\varOmega}{\nu} \right)^{4/3}. \tag{1.4}$$

If we assume that this boundary layer stability applies to layers of finite thickness h, we can again treat the fluid volume as two opposed half-spaces, with a stable thermal boundary layer adjacent to each boundary. We must also make the same two assumptions made for the non-rotating case: (*a*) the temperature drop across the layer occurs predominantly in the boundary layers, $\Delta T \approx 2\Delta T_\delta$; and (*b*) heat is transferred primarily by conduction within the stable boundary layer, $\Delta T_\delta \approx q\delta/k$. We should note here that the quality of these assumptions is far less certain for rotating convection than for the non-rotating case (and we test these assumptions in § 3). The rotating convection boundary layer stability criterion (1.4) therefore becomes

$$Nu \approx (Ra/Ra_c)^3 \approx 0.0023\, Ra^3 E^4, \tag{1.5}$$

using $Ra_c = 7.6 E^{-4/3}$ (Chandrasekhar 1953).

The scaling exponent $\alpha = 3$ is, to our knowledge, larger than any empirical law proposed from heat transfer measurements in rotating systems (e.g. Liu & Ecke 1997, 2009; Christensen & Aubert 2006; Aurnou 2007; King *et al.* 2009, 2010), which typically fall in the range between $\alpha \approx 2/7$ (Julien *et al.* 1996) and $\alpha \approx 2$ (Sprague *et al.* 2006). This prediction is, however, similar to the theoretical scalings derived for $Pr = \infty$ by Chan (1974) and Riahi (1977) using upper-bound variational methods, and separately by the turbulence model of Canuto & Dubovikov (1998).

1.4. *Regime transition*

In order to test (1.5) systematically, the relative values of Ra and E necessary to maintain the dominance of the Coriolis force must first be quantified. That is, in order to predict the range of Ra at a given E for which convection is geostrophic, the transition between geostrophic and weakly rotating convection regimes must be determined. We argue here that the transition between geostrophic and non-rotating heat transfer behaviour is determined by the relative thicknesses of the thermal boundary layer and the Ekman boundary layer.

The Ekman layer is a mechanical boundary layer that develops in rapidly rotating flows in order to rectify the interior flow with the constant angular momentum of the boundary. Ekman layers have characteristic thickness $\delta_E \sim (\nu/\Omega)^{1/2} \sim E^{1/2}h$ (Greenspan 1968). Although the Coriolis force dominates the interior fluid, viscous forces are important within the thin Ekman layer. The geostrophic boundary layer stability analysis presented above assumes that the stabilizing force in the thermal boundary layer, δ, is the Coriolis force. Once $\delta < \delta_E$, however, viscous stabilization of convection becomes important within this marginally stable thermal boundary layer. In this case ($\delta < \delta_E$), the local critical Rayleigh number should revert to the constant value relevant for non-rotating, viscously stabilized fluids. Boundary layer stability therefore predicts that the transition from geostrophic to non-rotating heat transfer behaviour occurs when the thermal boundary layer becomes thinner than the Ekman layer. This transition argument provides a mechanism for the boundary layer transition hypothesis of King *et al.* (2009).

The transition between these regimes can be estimated by the intersection of scaling laws for the thicknesses of the Ekman layer and the non-rotating, thermal boundary layer. King *et al.* (2009) assume that the non-rotating thermal boundary layer scales as $\delta/h \sim Nu^{-1} \sim Ra^{-2/7}$. The thermal boundary layer should therefore cross the Ekman layer ($\delta_E/h \sim E^{1/2}$) when $Ra \sim E^{-7/4}$. Boundary layer stability analysis, however, suggests that we should instead scale the thermal boundary layer as $\delta/h \sim Ra^{-1/3}$ (1.2). Furthermore, this 1/3 scaling for the thermal boundary layer thickness is more likely to apply to asymptotically high-Ra convection than a 2/7 law, which has a limited range of applicability (e.g. Ahlers *et al.* 2009). Assuming this non-rotating thermal boundary layer thickness scaling, we predict that the transition should occur when $\delta/\delta_E \sim Ra^{-1/3}E^{-1/2} = O(1)$, and therefore when

$$Ra\, E^{3/2} = O(1). \tag{1.6}$$

Essentially, this scaling predicts that the geostrophic style of heat transfer will break down when the Ekman boundary layer becomes thermally unstable. Interestingly, the predicted transition does not explicitly depend on the nature of the mechanical boundary conditions (cf. Schmitz & Tilgner 2009). Furthermore, this transition parameter scaling is similar to upper bounds for geostrophic convection predicted by other means (Chan 1974; Sakai 1997; Canuto & Dubovikov 1998).

Our hypotheses are the following: (i) geostrophic convection occurs in the range $Ra_c\,(= 7.6E^{-4/3}) \lesssim Ra \lesssim E^{-3/2}$; and (ii) convection in this regime transports heat according to the scaling law (1.5). Below, we argue that laboratory and numerical data support the use of the $Ra\, E^{3/2}$ regime transition parameter. We then use this transition parameter to distinguish and collapse geostrophic heat transfer data in order to test the proposed scaling (1.5) with heat transfer data predominantly from numerical simulations.

2. Methods

We test the scalings presented in § 1 using a suite of 84 numerical simulations and 117 laboratory experiments of rotating convection. Below, we describe the simulations that constitute the majority of our geostrophic convection data, and briefly describe the laboratory experiments, further details of which can be found in the supplementary material available at journals.cambridge.org/flm. Parameter ranges are given in table 1.

2.1. *Numerical simulations*

Direct numerical simulations are carried out by solving the Boussinesq momentum equation, continuity equation and energy equation in a Cartesian box. The domain has periodic sidewalls in order to approximate a horizontal layer of infinite extent. Top and bottom boundaries are rigid, no-slip and isothermal, with an imposed adverse temperature difference of ΔT, width-to-height aspect ratios $1 \leqslant \varGamma \leqslant 4$ and resolutions of up to $576 \times 576 \times 513$.

The code has been validated through comparison with results from linear theory and previously reported convection simulations, as well as through checks of internal consistency. First, we accurately reproduce the critical Rayleigh numbers and growth rates predicted by Chandrasekhar (1961). Results obtained with the present code are found to be in good agreement with simulation data produced by the independent finite volume code used in Stellmach & Hansen (2004). We also compare our results against those of Kunnen, Geurts & Clercx (2006), who report that, for $E = 4.714 \times 10^{-4}$, $Pr = 1$ and $Ra = 2.53 \times 10^6$, the time-averaged root mean square (r.m.s.) vertical velocity and temperature fluctuations at the mid-plane are 174.97 and 0.0793. We find values of 173.37 and 0.0789 for identical parameters, which agree to within 1 %. Finally, we compare our results for non-rotating convection against values for the Nusselt number, as well as toroidal and poloidal energies, given by Hartlep (2004), again finding agreement to within 1 %.

To test resolution requirements, we systematically varied the grid size for selected parameter values. Care needs to be taken in order to resolve the thin Ekman boundary layers. As an example, figure 1 shows time series of Nusselt numbers computed at various spatial resolutions for the special case $E = 10^{-5}$, $Ra = 7 \times 10^7$ and $Pr = 7$. Mean values for the most important diagnostic parameters used in the main part of this paper are compiled in table 2. For grids exceeding $96 \times 96 \times 65$ points, the computed values are fairly accurate. The Chebyshev basis functions used for vertical discretization naturally provide high resolution close to the boundaries and are thus well suited for resolving thin boundary layers. In the simulations used for our study, care has been taken to ensure that at least seven vertical grid levels are present within the Ekman layers.

A further consistency check is provided by the energy balance. If temperature is scaled by ΔT, length by h and velocity by κ/h, the top, bottom and volume-averaged Nusselt numbers are defined as

$$Nu_t := -\left\langle \frac{\partial T}{\partial z} \right\rangle\bigg|_{z=1}, \quad Nu_b := -\left\langle \frac{\partial T}{\partial z} \right\rangle\bigg|_{z=0}, \quad Nu_v := \left\langle u_z T - \frac{\partial T}{\partial z} \right\rangle_{\mathscr{V}}, \tag{2.1}$$

respectively, where $\langle \cdots \rangle_{\mathscr{V}}$ denotes a volume average. Viscous dissipation is defined as

$$D_{visc} := Pr\, \langle (\nabla \times \boldsymbol{u})^2 \rangle_{\mathscr{V}} . \tag{2.2}$$

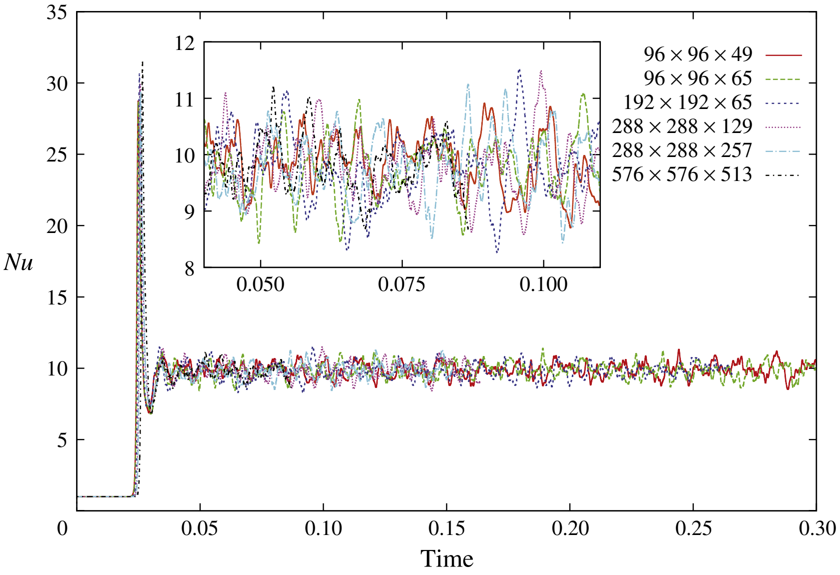

FIGURE 1. (Colour online available at journals.cambridge.org/flm) Nusselt number versus time for $E = 10^{-5}$, $Pr = 7$, $Ra = 7 \times 10^7$ and an aspect ratio of unity for different resolutions ranging from 96 × 96 × 48 to 576 × 576 × 513 grid points. All runs were started from a static, isothermal state superposed with small random perturbations. Time is normalized by the thermal diffusion time scale, h^2/κ.

N_x	N_y	N_z	$(\Delta T)_{av}$	Nu	u_{rms}	δ_E	δ
96	96	49	0.221	9.86	415.6	1.06×10^{-2}	3.71×10^{-2}
96	96	65	0.362	9.84	414.8	1.00×10^{-2}	3.73×10^{-2}
192	192	65	0.169	9.83	415.0	1.00×10^{-2}	3.74×10^{-2}
288	288	128	0.108	9.85	415.4	1.00×10^{-2}	3.74×10^{-2}
288	288	256	0.100	9.84	415.1	1.00×10^{-2}	3.76×10^{-2}
576	576	513	0.040	9.83	414.9	1.00×10^{-2}	3.77×10^{-2}

TABLE 2. Resolution test for the case $E = 10^{-5}$, $Pr = 7$ and $Ra = 7 \times 10^7$. All runs were started from a stationary, isothermal state onto which small random thermal perturbations have been superimposed. After an initial transient, a statistically stationary state is reached. The reported Nusselt numbers Nu and the r.m.s. velocities u_{rms} are values obtained by averaging the time series over a time interval $(\Delta T)_{av}$. The Ekman layer thickness δ_E is defined by the location of the maximum of the r.m.s. horizontal velocity. The edge of the thermal boundary layer thickness δ is defined by the location at which the variance of the temperature fluctuations attains its maximum.

Conservation of energy requires that

$$Nu := \overline{Nu}_t = \overline{Nu}_b = \overline{Nu}_v \tag{2.3}$$

and

$$\overline{D}_{visc} = Pr\, Ra\, (Nu - 1), \tag{2.4}$$

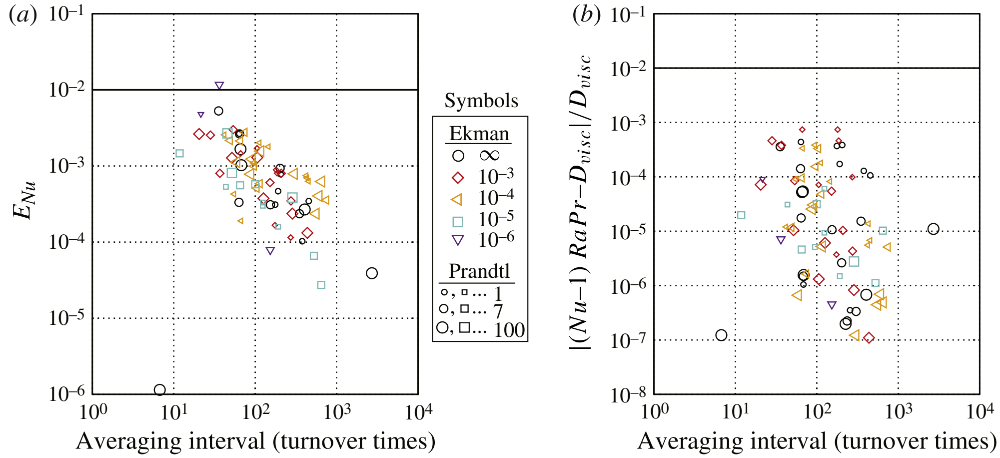

FIGURE 2. (Colour online) Consistency checks for the performed simulations, where the conditions (2.3) and (2.4) are compared with simulation data in (*a*) and (*b*), respectively. The notation $E_{Nu} = \max(|\overline{Nu}_b - \overline{Nu}_t|, |\overline{Nu}_b - \overline{Nu}_v|, |\overline{Nu}_t - \overline{Nu}_v|)/(\overline{Nu}_v - 1)$ is used for brevity. The solid horizontal lines indicate the 1 % error level. Note that there is a trend for the error to decrease with increasing length of the averaging interval measured in terms of turnover times.

where the overbar denotes a temporal average (Siggia 1994). Note that these relations formally hold if the temporal average is taken over an infinite time interval. Figure 2 shows that, for the finite time series computed for this study, the errors in the above relations are below 1 %, with the exception of one case ($E = 10^{-6}$, $Pr = 7$, $Ra = 2.1 \times 10^8$), which has a maximum Nusselt number error of 1.1 %. These low errors indicate that a statistically stationary state has been reached and that the solutions are in thermal and energetic equilibrium. Also, as expected, the error tends to decrease with the length of the simulated time series. Since energy is not discretely conserved by the chosen Chebyshev discretization, the results shown in figure 2 provide a useful check for our simulations.

2.2. *Laboratory experiments*

Laboratory experiments are carried out in a 20 cm diameter cylindrical tank of water ($4.5 \lesssim Pr \lesssim 7$) or sucrose solution ($6 \lesssim Pr \lesssim 11$) that is heated from below and rotated about a vertical axis. The tank height (h) varies from 3.2 to 20 cm, permitting a broad range of accessible Ra and E. The temperature drop across the fluid layer (ΔT) is measured by two arrays of six thermistors within the top and bottom tank endwalls. Heat flux (q) is measured as the electrical power supplied to the resistance heating element divided by its area, and is compared with measurements of heat absorbed by a heat exchanger above the tank. Input heat flux is limited to $q > 300$ W m^{-2}, such that estimated errors in Nu measurements are never more than 30 %. The entire tank set-up is insulated with 20 cm of closed-cell foam and is rotated up to 50 times per minute.

We define RBC as convection in a horizontal layer of infinite extent, but experimental practice requires that the container be bounded by sidewalls. In rotating convection experiments, subcritical convection modes are observed to emerge near the tank sidewalls (Liu & Ecke 1999). These sidewall modes can contribute to heat transport even beyond the onset of bulk convection, complicating the use of simple scalings intended for bulk modes alone. Although no general treatment of

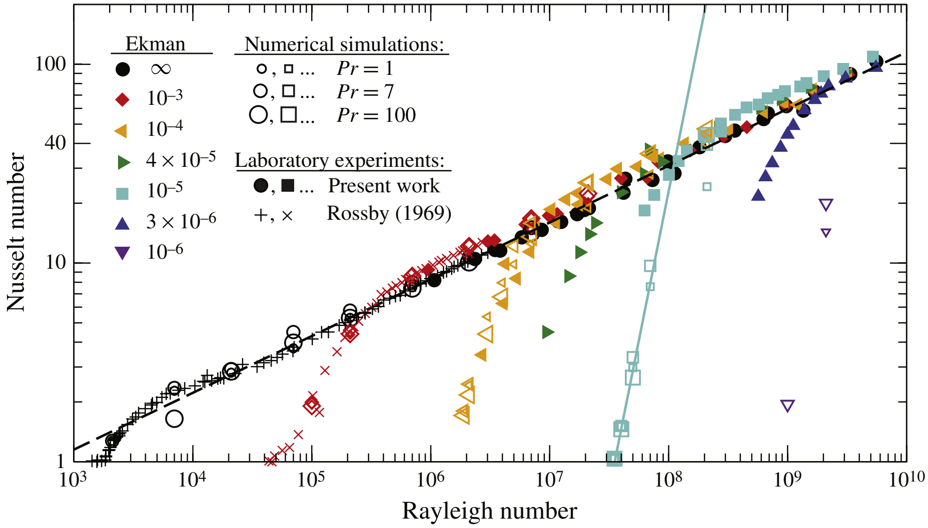

FIGURE 3. (Colour online) Nusselt number plotted versus Rayleigh number. Seven different Ekman numbers are explored, indicated by various symbol shapes. Solid symbols indicate measurements from laboratory experiments. Open symbols indicate results from numerical simulations, with symbol size corresponding to Pr. The Ekman number values are approximate for laboratory experiments, which vary due to changes in fluid viscosity. Data from Rossby (1969) are also shown for comparison for non-rotating (+) and $E \approx 10^{-3}$ (×) cases. The dashed black line represents the non-rotating scaling $Nu = 0.16\,Ra^{2/7}$. The solid line illustrates the rapidly rotating scaling (1.5) for $E = 10^{-5}$.

the contribution of such modes to fully developed convective heat transport exists, previous experimental surveys find that evidence of sidewall modes in heat transport is limited to $Nu \lesssim 3$ (e.g. Rossby 1969; Zhong, Ecke & Steinberg 1993). Our rotating convection experiments have $Nu > 3.5$. Furthermore, the minimum Nusselt number that we access increases sharply as we move to tanks with smaller aspect ratio, in which significant sidewall modes are more likely (Liu & Ecke 1999): for $\Gamma \lesssim 4$, $Nu \gtrsim 4.5$; for $\Gamma \lesssim 2$, $Nu \gtrsim 18$; and for $\Gamma \approx 1$, $Nu \gtrsim 21$. We do not, then, anticipate that sidewall modes contribute significantly to heat transport in our experiments. Furthermore, where they overlap, our experimental and numerical data are generally in agreement. Because sidewall modes are not possible in the simulations, this agreement indicates that such modes are not of paramount importance in the present experimental measurements.

Additional information on laboratory experiments is given in the supplementary material.

3. Results

Figure 3 shows heat transfer behaviour, Nu versus Ra, for various E. We first examine non-rotating ($E = \infty$) heat transfer to provide a baseline for rotating convection. Combining data from the present study with that from Rossby (1969), we have 84 non-rotating convection cases in the range $10^4 < Ra < 10^{10}$, which yield a best-fit scaling law of $Nu = 0.162(\pm 0.006)Ra^{0.284(\pm 0.002)}$. This relationship is in close agreement with heat transfer scalings found at similar parameters in previous work (Chilla *et al.* 1993; Cioni, Ciliberto & Sommeria 1997; Liu & Ecke 1997). This

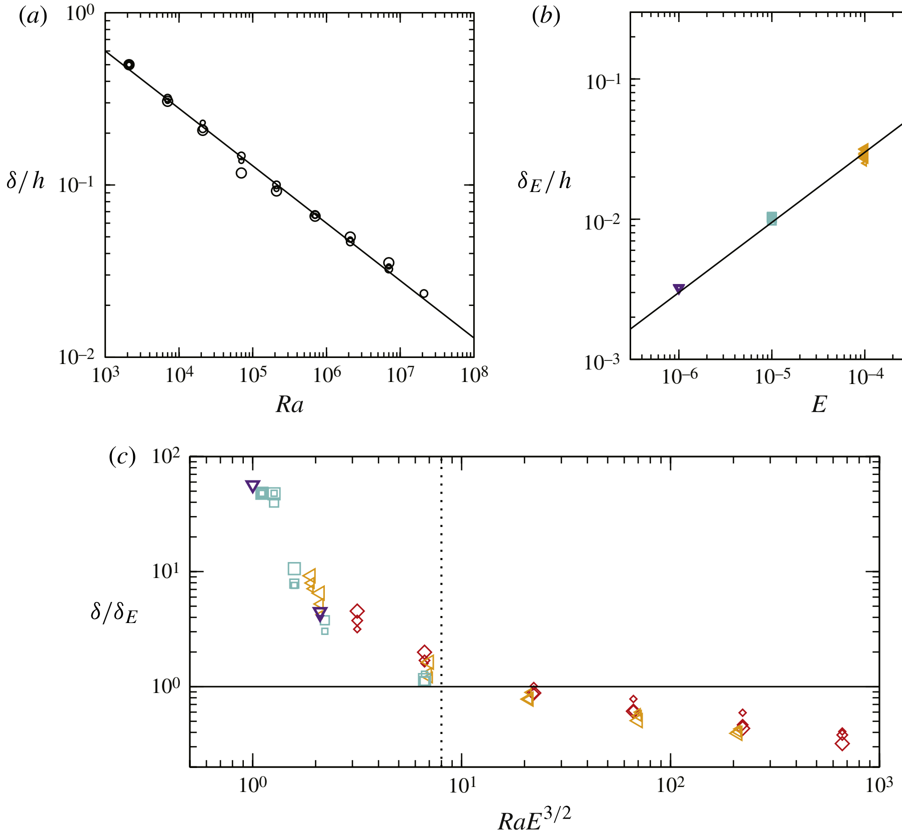

FIGURE 4. (Colour online) (*a*) Thermal boundary layer thicknesses, δ, versus Ra from numerical simulations of non-rotating convection. The line shows the best-fit scaling $\delta = 5.7\,Ra^{0.33}$. (*b*) Velocity boundary layer thickness calculations versus E from numerical simulations of rotating convection. The line shows the scaling $\delta_E = 3E^{1/2}$. (*c*) The ratio of thermal to Ekman boundary layer thickness, δ/δ_E, from rotating convection simulations plotted versus the predicted transition parameter, $Ra\,E^{3/2}$. The vertical dotted line shows the crossing prediction from the intersection of the scalings in (*a*) and (*b*). Symbols carry the same meaning as in figure 3.

scaling can be approximated as $Nu = 0.16\,Ra^{2/7}$, which is indicated by the dashed black line in figure 3.

Rotating convection heat transfer data exhibit first-order characteristics similar to those seen in previous studies (e.g. Rossby 1969). First, the onset of convection occurs at higher Rayleigh numbers for decreasing Ekman numbers. Beyond this critical Rayleigh number, heat transfer grows increasingly convective, yet remains suppressed below the Nusselt numbers found in non-rotating convection. Above a transitional Rayleigh number, the heat transfer data for each Ekman number briefly overshoot (e.g. Liu & Ecke 2009; Zhong, Stevens & Clercx 2009) and then roughly conform to the non-rotating behaviour, where the E dependence is weak. Where laboratory and numerical data overlap, they are typically in good agreement. The steep, solid line in figure 3 shows the predicted geostrophic scaling law (1.5) for $E = 10^{-5}$.

In figure 4, we examine calculations of boundary layer thicknesses from numerical simulations. Ekman (thermal) boundary layer thicknesses are calculated as the mean

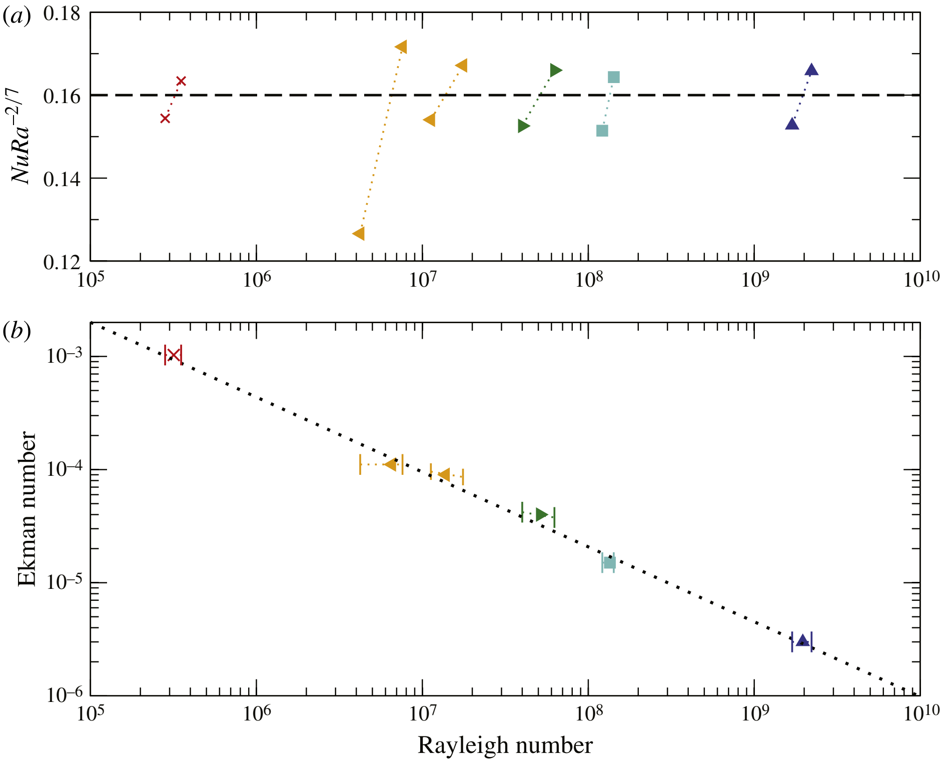

FIGURE 5. (Colour online) (*a*) Selected experimental heat transfer data normalized by the non-rotating scaling $Ra^{2/7}$ plotted versus Ra to determine transition locations. Symbols are the same as in figure 3. The horizontal, dashed black line shows the empirical non-rotating scaling law, $Nu = 0.16\,Ra^{2/7}$. (*b*) Transition locations from (*a*) plotted in Ekman–Rayleigh space. The dotted line shows the best-fit power law, $Ra_t = 10E^{-3/2}$. Symbols carry the same meaning as in figure 3.

vertical distances of the first local maximum of the horizontally averaged velocity (temperature) variance interior to the top and bottom domain boundaries (Belmonte, Tilgner & Libchaber 1994). Figure 4(*a*) shows the thicknesses of thermal boundary layers versus Ra from simulations of non-rotating convection. A best-fit scaling yields $\delta/h = 5.7(\pm 0.7)Ra^{-0.33(\pm 0.01)}$, in agreement with the prediction from marginal boundary layer stability analysis (1.2). Figure 4(*b*) shows calculations of Ekman boundary layer thicknesses versus E from rotating convection simulations. The solid line shows $\delta_E/h = 3E^{1/2}$ (Greenspan 1968), which fits the data to within 8 % on average for $E \leqslant 10^{-4}$. Equating the scalings for each boundary layer, we expect that they cross when $Ra \approx 8E^{-3/2}$, in agreement with the prediction (1.6). The ratio of thermal to Ekman boundary layer thickness is shown in figure 4(*c*) versus $Ra\,E^{3/2}$ for all rotating RBC simulations, and the predicted crossing is indicated by the dotted vertical line. The boundary layers are, in fact, observed to cross somewhere in the range $6 \lesssim Ra\,E^{3/2} \lesssim 20$.

In figure 5, we test the applicability of the regime transition prediction (1.6) to the heat transfer data. Figure 5(*a*) shows convective heat transfer data from laboratory experiments normalized by the empirical non-rotating scaling, $Nu\,Ra^{-2/7}$, plotted versus the Rayleigh number. Two data points from each of six different data sets for

$10^{-3} \lesssim E \lesssim 3 \times 10^{-6}$ are selected to quantify the regime transitions. Laboratory data are used exclusively because of their higher density in Ra space within this parameter range. The data points chosen from each set are the closest two cases on either side of the transition, as defined by the first crossing of the non-rotating scaling law, $Nu = 0.16\, Ra^{2/7}$ (dashed line). (Two pairs are shown for $E \approx 10^{-4}$, which represent data from two separate convection tanks, and with slightly different E values.) The transition is approximated by the intersection of the non-rotating scaling (dashed line) with the line connecting the two data points from each pair in semi-log space (dotted lines).

Figure 5(*b*) shows the transition locations in Ra–E space. Error bounds illustrate the location of the data points on either side of the transition. A best-fit power-law regression yields a transitional Ekman number scaling of $E_t = 4.7(^{+2.5}_{-1.5}) Ra^{0.67(\pm 0.02)}$. Equivalently, this gives a transitional Rayleigh number scaling of $Ra_t = 10(^{+10}_{-4}) E^{1.50(\pm 0.06)}$, which is in agreement with the boundary layer transition prediction (1.6) and thickness measurements (figure 4). Thus, the heat transfer regime transitions are well described by the swapping of the nested thermal and Ekman boundary layers, and both occur near $Ra\, E^{3/2} \approx 10$.

We test the geostrophic heat transfer scaling (1.5) in figure 6. Figure 6(*a*) shows Nu data normalized using the standard RBC reduction, $Nu\, Ra^{-1/3}$ (Ahlers *et al.* 2009), plotted versus $Ra\, E^{3/2}$. This renormalization of the axes allows us to plot the predicted geostrophic scaling for all E using a single curve: (1.5) becomes $Nu\, Ra^{-1/3} = 0.0023\, (Ra\, E^{3/2})^{8/3}$ (solid line). In figure 6(*b*), heat transfer data normalized by the geostrophic scaling, $Nu\, Ra^{-3} E^{-4}$ are plotted versus $Ra\, E^{3/2}$. The geostrophic prediction (1.5) is again shown by the solid line. Figure 6(*c*) shows an expanded view of the region of figure 6(*b*) indicated by the grey box.

The most rapidly rotating data presented in figure 6 appear to conform to the predicted geostrophic law. Indeed, the 22 convection cases with lowest $Ra\, E^{3/2}$ (< 2.7) are best fit by $Nu\, Ra^{-3} E^{-4} = 0.0023(\pm 0.0002)\, (Ra\, E^{3/2})^{0(\pm 0.1)}$, in line with geostrophic scaling law (1.5). Thus, our most rapidly rotating convection data, most of which come from numerical simulations, are in good agreement with the prediction from boundary layer stability analysis.

This agreement between theory and experiment (both computational and laboratory) is contingent upon the quality of the assumptions on which the theory relies. The two assumptions made to arrive at (1.5) from (1.4) – that convective heat transfer is ineffective in the thermal boundary layer, and that the temperature drop outside of the boundary layers is negligible – are less well tested for rotating convection than for non-rotating convection (e.g. Boubnov & Golitsyn 1990; Belmonte, Tilgner & Libchaber 1993; Julien *et al.* 1996). We can quantify the quality of these two assumptions using results from numerical simulations. We test each assumption using mean thermal profiles from simulations within the geostrophic regime, $Ra\, E^{3/2} < 10$. A test of the first assumption, $2\Delta T_\delta = \Delta T$, is given by $2\Delta T_\delta = 0.7(\pm 0.4)\Delta T$, indicating that total temperature drop does not always occur predominantly within the boundary layers. Similarly, we can test the second assumption, $\Delta T_\delta \approx q\delta/k$, finding $\Delta T_\delta/\Delta T = 0.7(\pm 0.2)\delta Nu/h$. Thus, the temperature gradient in the boundary layers is not observed to be purely conductive. Though these errors can be significant, they may not be important for order-of-magnitude scaling analysis. Furthermore, the errors in each of these assumptions offset each other to some extent, such that $\delta = 1.0(\pm 0.6) h/(2Nu)$. It is unclear whether these assumptions hold as $E \to 0$.

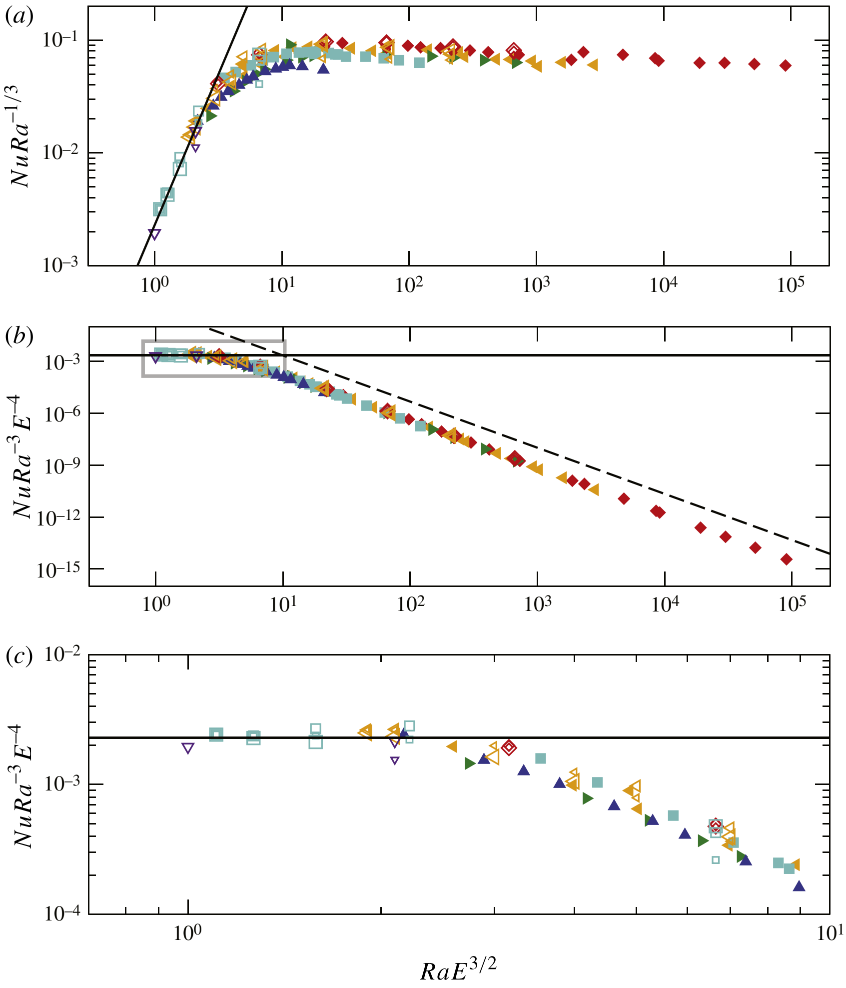

FIGURE 6. (Colour online) (*a*) The reduced Nusselt number, $Nu\,Ra^{-1/3}$, plotted versus the transition parameter, $Ra\,E^{3/2}$. Symbols are the same as in figure 3. The solid line shows the geostrophic heat transfer scaling prediction (1.5). (*b*) Heat transfer data normalized by the geostrophic scaling, $Nu\,Ra^{-3}E^{-4}$, shown versus $RaE^{3/2}$. The solid, horizontal line shows the exact scaling prediction (1.5). (*c*) Expanded view of the region of (*b*) indicated by the grey box. Symbols carry the same meaning as in figure 3.

4. Conclusions

Following the seminal work by Malkus (1954), we develop dimensional arguments for marginal boundary layer stability in geostrophic convection that produce a heat transfer scaling law $Nu \approx (Ra/Ra_c)^3 = 0.0023\,Ra^3E^4$. We also develop a transition parameter $Ra\,E^{3/2}$ that separates geostrophic and non-rotating styles of convective heat transfer.

We present data from numerical simulations and laboratory experiments in support of the geostrophic heat transfer scaling (figure 6). This scaling relationship is steeper than those proposed by previous experimental measurements, which is probably due to the fact that rapidly rotating convection has not been well explored. Indeed, this work is among the first to survey rapidly rotating ($E \leqslant 10^{-4}$), geostrophic ($Ra\,E^{3/2} < 10$)

RBC to date (cf. Liu & Ecke 2009; Schmitz & Tilgner 2010). We have not, however, acquired enough data at low $Ra\,E^{3/2}$ to verify or reject unequivocally the predicted heat transfer law (1.5). In particular, it should be noted that, of the 25 data points with $Ra\,E^{3/2} < 2.7$ used to test the geostrophic scaling, 23 come from numerical simulations, as the laboratory experiments are limited by heat flux considerations. Bigger, better-controlled experiments are needed to access this regime while simultaneously minimizing the role of sidewall modes. Generally, in order to test this prediction more conclusively, convection experiments and/or simulations must be realized at lower Ekman numbers such that ample data become available for $Ra\,E^{3/2} \lesssim 1$.

The transition parameter $Ra\,E^{3/2}$ relates the relative thicknesses of the thermal and Ekman boundary layers (figure 4) and aptly describes the transition between geostrophic and weakly rotating convection regimes (figure 5). The development of this parameter follows from dimensional analysis of boundary layer stability, arguing that the transition from geostrophic to weakly rotating convection occurs when the thermal boundary layer becomes thinner than the Ekman layer. This proposed transition mechanism is in agreement with the boundary layer control hypothesis proposed by King *et al.* (2009), and, furthermore, is not contingent upon the nature of the mechanical boundary conditions. In King *et al.* (2009), however, the use of an empirical scaling for non-rotating heat transfer gives a transition parameter of $Ra\,E^{7/4}$, which is unlikely to hold for Rayleigh–Bénard convection with extreme Ra and E values. Here, we show that these two boundary layers have thicknesses that scale as $\delta \propto Ra^{-1/3}h$ and $\delta_E / \propto E^{1/2}h$, respectively. Though based on the same premise, the resulting transition parameter $Ra\,E^{3/2}$ differs considerably from that developed in King *et al.* (2009).

Interestingly, the important dimensional quantities for which we seek scaling laws, heat flux q, thermal boundary layer thickness δ and Ekman layer thickness δ_E, are all predicted to follow scalings that are independent of the total layer height, h. Furthermore, since both boundary layer thickness scalings are depth-independent, the regime of convective heat transfer, determined by the ratio δ/δ_E, is also insensitive to h. Arguments for depth-independent heat transfer behaviour in non-rotating convection are not new (e.g. Priestley 1954; Spiegel 1971), and follow from the assumption that RBC behaves like two opposed, infinite half-spaces. If correct, depth-independent behaviour in turbulent, rapidly rotating RBC would help refine our understanding of this system.

Acknowledgements

EMK acknowledges the support of the Miller Institute for Basic Research in Science. JMA was funded by the NSF Geophysics Program (EAR-0944312) and NASA Planetary Atmospheres Program (NNX09AB61G). Computing resources were provided by the John von Neumann Institute for Computing.

Supplementary material is available at journals.cambridge.org/flm.

REFERENCES

Ahlers, G., Grossmann, S. & Lohse, D. 2009 Heat transfer and large scale dynamics in turbulent Rayleigh–Bénard convection. *Rev. Mod. Phys.* **81**, 503–537.

Amati, G., Koal, K., Massaioli, F., Sreenivasan, K. R. & Verzicco, R. 2005 Turbulent thermal convection at high Rayleigh numbers for a Boussinesq fluid of constant Prandtl number. *Phys. Fluids* **17**, 121701.

AURNOU, J. 2007 Planetary core dynamics and convective heat transfer scaling. *Geophys. Astrophys. Fluid Dyn.* **101** (5–6), 327–345.

BELMONTE, A., TILGNER, A. & LIBCHABER, A. 1993 Boundary layer length scales in thermal turbulence. *Phys. Rev. Lett.* **70** (26), 4067–4070.

BELMONTE, A., TILGNER, A. & LIBCHABER, A. 1994 Temperature and velocity boundary layers in turbulent convection. *Phys. Rev.* E **50** (1), 269–280.

BOUBNOV, B. & GOLITSYN, G. 1990 Temperature and velocity-field regimes of convective motions in a rotating plane fluid layer. *J. Fluid Mech.* **219**, 215–239.

CANUTO, V. & DUBOVIKOV, M. 1998 Two scaling regimes for rotating Rayleigh–Bénard convection. *Phys. Rev. Lett.* **80** (2), 281–284.

CASTAING, B., GUNARATNE, G., HESLOT, F., KADANOFF, L., LIBCHABER, A., THOMAE, S., WU, X. Z., ZALESKI, S. & ZANETTI, G. 1989 Scaling of hard turbulence in Rayleigh–Bénard convection. *J. Fluid Mech.* **204**, 1–30.

CHAN, S.-K. 1974 Investigation of turbulent convection under a rotational constraint. *J. Fluid Mech.* **64** (3), 477–506.

CHANDRASEKHAR, S. 1953 The instability of a layer of fluid heated below and subject to Coriolis forces. *Proc. R. Soc. Lond.* A **217** (1130), 306–327.

CHANDRASEKHAR, S. 1961 *Hydrodynamic and Hydromagnetic Stability*. Clarendon Press.

CHILLA, F., CILIBERTO, S., INNOCENTI, C. & PAMPALONI, E. 1993 Boundary layer and scaling properties in turbulent thermal convection. *Il Nuovo Cimento* D **15D** (9), 1229–1249.

CHRISTENSEN, U. & AUBERT, J. 2006 Scaling properties of convection-driven dynamos in rotating spherical shells and application to planetary magnetic fields. *Geophys. J. Intl* **166** (1), 97–114.

CIONI, S., CILIBERTO, S. & SOMMERIA, J. 1997 Strongly turbulent Rayleigh–Bénard convection in mercury: comparison with results at moderate Prandtl number. *J. Fluid Mech.* **335**, 111–140.

GLAZIER, J., SEGAWA, T., NAERT, A. & SANO, M. 1999 Evidence against ‘ultrahard’ thermal turbulence at very high Rayleigh numbers. *Nature* **398**, 307–310.

GREENSPAN, H. 1968 *The Theory of Rotating Fluids*. Cambridge University Press.

HARTLEP, T. 2004 Strukturbildung und Turbulenz. Eine numerische Studie zur turbulenten Rayleigh–Bénard Konvektion. PhD thesis, Mathematisch-Naturwissenschaftliche Fakultät, Universität Göttingen.

JULIEN, K., LEGG, S., MCWILLIAMS, J. & WERNE, J. 1996 Rapidly rotating turbulent Rayleigh–Bénard convection. *J. Fluid Mech.* **322**, 243–273.

KING, E., SODERLUND, K., CHRISTENSEN, U. R., WICHT, J. & AURNOU, J. M. 2010 Convective heat transfer in planetary dynamo models. *Geochem. Geophys. Geosyst.* **11** (6), Q06016.

KING, E., STELLMACH, S., NOIR, J., HANSEN, U. & AURNOU, J. 2009 Boundary layer control of rotating convection systems. *Nature* **457** (7227), 301–304.

KUNNEN, R. P. J., GEURTS, B. J. & CLERCX, H. J. H. 2006 Direct numerical simulation of turbulent rotating Rayleigh–Bénard convection. In *Direct and Large-Eddy Simulation VI, 12–14 September 2005, Poitiers, France*, *ERCOFTAC Ser.*, 10. pp. 233–240. Springer.

LIU, Y. M. & ECKE, R. E. 1997 Heat transport scaling in turbulent Rayleigh–Bénard convection: effects of rotation and Prandtl number. *Phys. Rev. Lett.* **79** (12), 2257–2260.

LIU, Y. & ECKE, R. E. 1999 Nonlinear travelling waves in rotating Rayleigh–Bénard convection: stability boundaries and phase diffusion. *Phys. Rev.* E **59** (4), 4091–4105.

LIU, Y. & ECKE, R. 2009 Heat transport measurements in turbulent rotating Rayleigh–Bénard convection. *Phys. Rev.* E **80** (3), 6314–6325.

MALKUS, W. V. R. 1954 The heat transport and spectrum of thermal turbulence. *Proc. R. Soc. Lond.* A **225** (1161), 196–212.

NIEMELA, J. J. & SREENIVASAN, K. R. 2006 Turbulent convection at high Rayleigh numbers and aspect ratio 4. *J. Fluid Mech.* **557**, 411–422.

PELLEW, A. & SOUTHWELL, R. 1940 On maintained convective motion in a fluid heated from below. *Proc. R. Soc. Lond.* A **176**, 312–343.

PRIESTLEY, C. 1954 Convection from a large horizontal surface. *Austral. J. Phys.* **7**, 176–202.

RIAHI, N. 1977 Upper-bound problem for a rotating system. *J. Fluid Mech.* **81** (3), 523–528.

ROSSBY, H. 1969 A study of Bénard convection with and without rotation. *J. Fluid Mech.* **36** (2), 309–335.

SAKAI, S. 1997 The horizontal scale of rotating convection in the geostrophic regime. *J. Fluid Mech.* **333**, 85–95.

SCHMITZ, S. & TILGNER, A. 2009 Heat transport in rotating convection without Ekman layers. *Phys. Rev.* E **80** (1), 5305–5307.

SCHMITZ, S. & TILGNER, A. 2010 Transitions in turbulent rotating Rayleigh–Bénard convection. *Geophys. Astrophys. Fluid Dyn.* **104** (5–6), 481–489.

SIGGIA, E. D. 1994 High Rayleigh number convection. *Annu. Rev. Fluid Mech.* **26**, 137–168.

SPIEGEL, E. 1971 Convection in stars. I. Basic Boussinesq convection. *Annu. Rev. Astron. Astrophys.* **9**, 323–352.

SPRAGUE, M., JULIEN, K., KNOBLOCH, E. & WERNE, J. 2006 Numerical simulation of an asymptotically reduced system for rotationally constrained convection. *J. Fluid Mech.* **551**, 141–174.

STELLMACH, S. & HANSEN, U. 2004 Cartesian convection-driven dynamos at low Ekman number. *Phys. Rev.* E **70**, 056312.

SUN, C., CHEUNG, Y. H & XIA, K.-Q. 2008 Experimental studies of the viscous boundary layer properties in turbulent Rayleigh–Bénard convection. *J. Fluid Mech.* **605**, 79–113.

ZHONG, F., ECKE, R. E. & STEINBERG, V. 1993 Rotating Rayleigh–Bénard convection: asymmetric modes and vortex states. *J. Fluid Mech.* **249**, 135–159.

ZHONG, J., STEVENS, R. & CLERCX, H. 2009 Prandtl-, Rayleigh-, and Rossby-number dependence of heat transport in turbulent rotating Rayleigh–Bénard convection. *Phys. Rev. Lett.* **102**, 044502.

Supplementary material for: "Heat transfer by rapidly rotating Rayleigh-Bénard convection"

E. M. KING[1], **S. STELLMACH**[2], AND **J. M. AURNOU**[3]

[1]Department of Earth and Planetary Science, University of California, Berkeley, 94720-4767
USA

[2]Institut für Geophysik, WWU Münster, AG Geodynamik Corrensstr. 24, Münster, 48149
Germany

[3]Department of Earth and Space Sciences, University of California, Los Angeles, 90095-1567
USA

(Received February 2, 2011)

Here, we provide supplementary material on the experimental methods for "Heat transfer by rapidly rotating Rayleigh-Bénard convection". Section 1 provides a detailed description of the laboratory experiment, and section 2 tabulates heat transfer data from laboratory.

1. Laboratory Experiments

1.1. *Experimental Apparatus*

Laboratory experiments are carried out in cylindrical tanks of water or sucrose solution using the rotating magnetoconvection device (RoMag) at UCLA (King 2009). The experimental convection setup is shown in figure 1, and consists of a cylindrical convection tank that sits atop a rotating pedestal. The convection tank is 20 cm in diameter, and has variable height, from 3.2 cm to 20 cm such that the diameter to height aspect ratio is in the range $1 \leq \Gamma \leq 6.25$. Increasing the tank's height increases Ra (as h^3) and decreases E (as h^{-2}).

The tank is heated from below by an electrical heating element and cooled from above by a thermstated heat exchanger. The bottom thermal boundary condition is therefore one of constant heat flux, rather than of constant temperature, as in the numerical simulations. This means that, experimentally, we fix flux-Rayleigh numbers, $Rf = RaNu$, instead of the traditional Rayleigh numbers that are fixed in the numerical simulations. Despite this difference in boundary conditions, mean convective behavior does not strongly vary between the two types of thermal boundary conditions (e.g., Johnston & Doering 2009; King *et al.* 2009).

Convection experiments are carried out near room temperature and the apparatus is surrounded by roughly 20 cm of closed cell foam insulation to minimize ambient thermal interaction. The cylinder sidewalls are polycarbonate, and the top and bottom tank endwalls are thin layers of either copper or aluminum, designed to minimize thermal heterogeneity within the boundaries. The importance of finite conductivity is characterized by the Biot number, $Bi = Nu \frac{k_{\mathrm{fluid}}}{H_{\mathrm{fluid}}} \frac{H_{\mathrm{boundary}}}{k_{\mathrm{boundary}}}$, where k is thermal conductivity and H is layer thickness. For the experiments presented here, $Bi < 0.1$, such that the influence of finite conductivity boundaries is small (Verzicco 2004).

Figure 2 shows a schematic of the heat delivery and removal system to the experimental apparatus. The heat required to drive convection is accomplished by a 16 Ohm mica

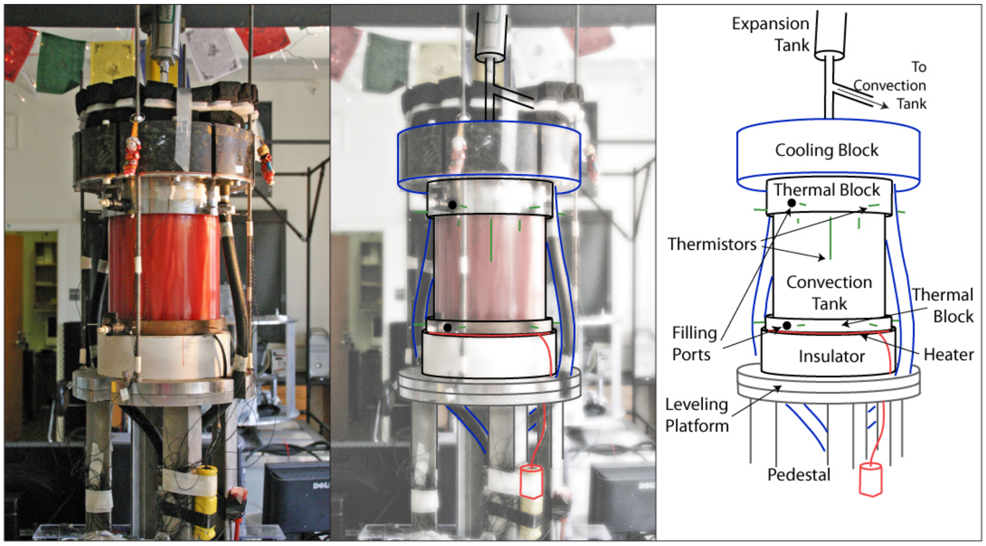

FIGURE 1. The convection tank setup of the rotating magnetoconvection device (RoMag). From bottom to top are the rotating pedestal, leveling platform, insulator, heater, bottom endwall, sidewall, top endwall, cooling block, and expansion tank.

resistance element. A direct current is passed through the heater by way of a 0-5 kW power supply, and is transmitted to the rotating frame by a system of 50 Amp solid-state slip rings. The heat produced below the convection tank is removed above the tank by a heat exchanging unit, referred to as the cooling block. Water is forced through the cooling block by a lab chiller that maintains a reservoir of treated water at a thermostated temperature. The chilled water is delivered into the rotating frame via a two-channel fluid rotary union. The cooling block is an aluminum (T6061) cylinder into which has been cut two double-wound spiral flow channels, such that the temperature distribution is roughly uniform. The heat absorbed by the lab chiller is removed by recirculation from an air-cooled industrial rooftop chiller.

The convection tank setup is rotated by a brushless (for rotation rate uniformity) servomotor. A lower table supporting the diagnostic instrumentation co-rotates such that sensitive signals need not be transmitted through noise inducing slip rings. The rotation rate is limited to 50 rotations per minute, such that the maximum strength of centrifugation within the convection container is never more than 30% gravitational acceleration (Lopez & Marques 2009).

1.2. *Fluid Properties*

Working fluids are water and sucrose solution, whose typical thermophysical properties are listed in Table 1, and the temperature dependence thereof is given below.

The properties of water, in SI units (given in table 1), are (Lide 2000):

$$\rho = 999.8 + 0.1041T - 9.718 \times 10^{-3}T^2 + 5.184 \times 10^{-5}T^3 \tag{1.1}$$

$$\alpha_T = -6.82 \times 10^{-5} + 1.70 \times 10^{-5}T - 1.82 \times 10^{-7}T^2 + 1.05 \times 10^{-9}T^3 \tag{1.2}$$

$$\kappa = 1.31210^{-7} + 6.97210^{-10}T - 5.63110^{-12}T^2 + 2.63310^{-14}T^3 \tag{1.3}$$

$$k = 0.5529 + 2.66210^{-3}T - 2.37410^{-5}T^2 + 1.10810^{-7}T^3 \tag{1.4}$$

$$C_P = \frac{k}{\rho\kappa}, \tag{1.5}$$

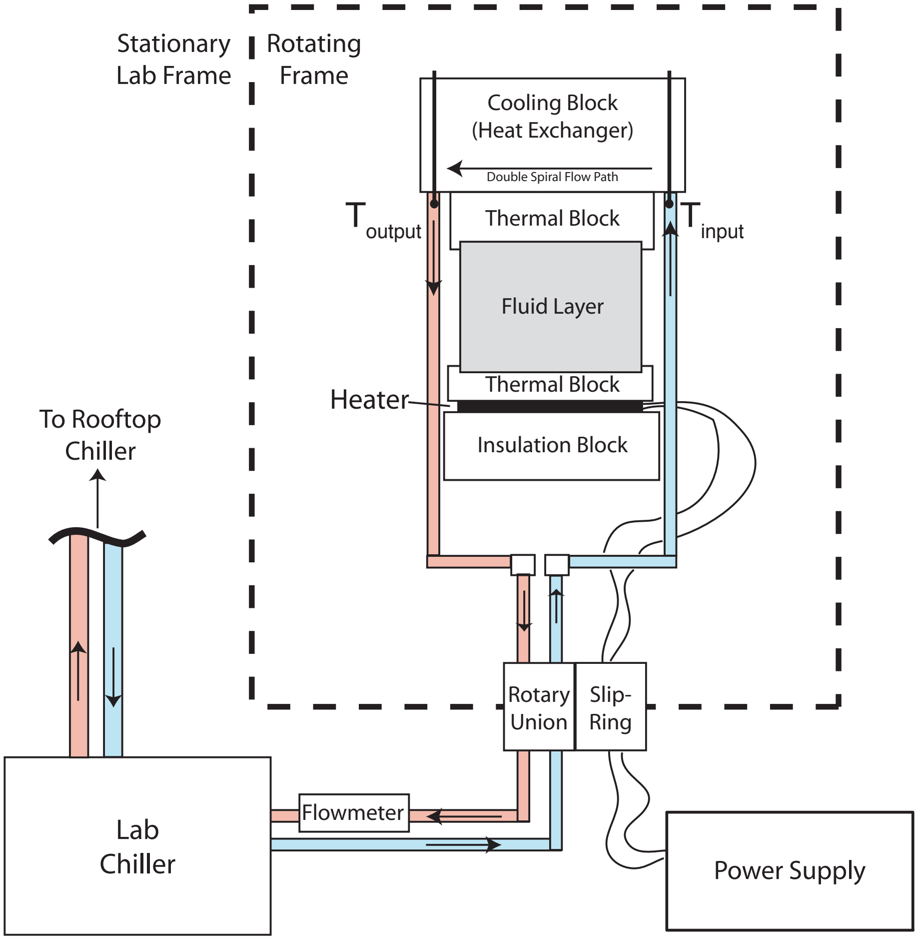

FIGURE 2. A schematic of RoMag's experimental thermal circulation system.

Property	Symbol	Units	Water	Sucrose Solution
density	ρ	kg/m^3	1000	1050
thermal expansivity	α_T	K^{-1}	2×10^{-4}	2×10^{-4}
viscous diffusivity	ν	m^2/s	10^{-6}	1.5×10^{-6}
thermal diffusivity	κ	m^2/s	1.4×10^{-7}	1.4×10^{-7}
Prandtl number	$Pr = \nu/\kappa$	—	7	11
specific heat	Cp	J/kg K	4180	3815
thermal conductivity	k	J/m s K	0.6	0.6

TABLE 1. Thermophysical properties of water (20°C) (Lide 2000) and sucrose solution (14.4% sugar by mass, 20°C) (Hirst & Cox 1976).

where T is the temperature of the fluid in °C.

In some convection cases, sugar is added to water to create a denser solution, which permits polystyrene micro-particles to remain in suspension for use with acoustic Doppler velocimetry. The properties of sucrose solution are essentially that of water with the added dependency of the concentration of sugar. By mass, the percentage of sugar to water in the solution is referred to as degrees Brix, °BX. The density of the solution is measured prior to conducting experiments, and variations about that density with temperature are assumed to be determined by the thermal expansivity of pure water given above. The remaining fluid properties of sucrose solution are (Hirst & Cox 1976):

$$\nu = (6.581/(((61.5 + T) - (1 + 0.011\,T)\,^{\circ}\mathrm{BX})^2))/\rho \tag{1.6}$$

$$\kappa = \frac{k}{\rho C_P} \tag{1.7}$$

$$\begin{aligned} k = 0.5758 + 1.360 \times 10^{-3}\,T - 3.006 \times 10^{-3}\,^{\circ}\mathrm{BX} - 2.511 \times 10^{-6}\,^{\circ}\mathrm{BX}\,T \\ -3.341 \times 10^{-6}\,^{\circ}\mathrm{BX}^2 - 1.182 \times 10^{-7}\,^{\circ}\mathrm{BX}^2\,T \end{aligned} \tag{1.8}$$

$$Cp = [1 - (0.632 - 0.001\,T)\,^{\circ}\mathrm{BX}/100]4184. \tag{1.9}$$

1.3. *Experimental Diagnostics*

Six thermistors are situated within each of the top and bottom boundaries, 2 mm from the fluid interface, at two-thirds the tank's radius. The probes are equally spaced in azimuth, forming six vertically aligned pairs. These thermistors measure the temperature difference across the fluid layer, ΔT. The heat flux, q, is measured as the power input to the resistor, and is compared, for accuracy, with the heating rate of coolant cycling through a thermostated bath atop the convection tank.

Figure 3 shows an example of temperature time series measurements from RoMag. Panels a) and b) show raw thermistor measurements from the top and bottom boundaries, respectively. These temperature measurements are denoted $T_i^{\mathrm{top}}(t)$ and $T_i^{\mathrm{bottom}}(t)$, where $i = 1, ..., 6$ corresponding to azimuthal location. From these measurements are calculated, for example, the mean fluid temperature, T_{fluid} (panel c)), and temperature drop, ΔT (panel d)). The mean temperature of the convecting fluid is calculated as

$$T_{\mathrm{fluid}} = \frac{1}{12}\left\langle \sum_{i=1}^{6} T_i^{\mathrm{top}}(t) + \sum_{i=1}^{6} T_i^{\mathrm{bottom}}(t) \right\rangle_t , \tag{1.10}$$

where $\langle\cdot\rangle_t$ represents time averaging. The mean temperature drop across the fluid layer is calculated as:

$$\Delta T = \frac{1}{6}\left\langle \sum_{i=1}^{6} T_i^{\mathrm{bottom}}(t) - \sum_{i=1}^{6} T_i^{\mathrm{top}}(t) \right\rangle_t . \tag{1.11}$$

2. Laboratory Data

Here, we provide a table of heat transfer data from laboratory experiments. The column headings have the following meaning: h is the height of the convection tank in meters; RPM is the rotation rate of the tank in rotations per minute; Power is the electrical power supplied to the heater in watts; Pr is the Prandtl number of the fluid; E is the Ekman number; Ra is the Rayleigh number; and Nu is the Nusselt number. Non-dimensional parameters are defined as $Pr = \nu/\kappa$, $E = \nu/2\Omega h^2$, $Ra = \alpha_T g \Delta T h^3/\nu\kappa$, and $Nu = qh/k\Delta T$, where ν is the fluid's kinematic viscosity, κ is the fluid's thermal

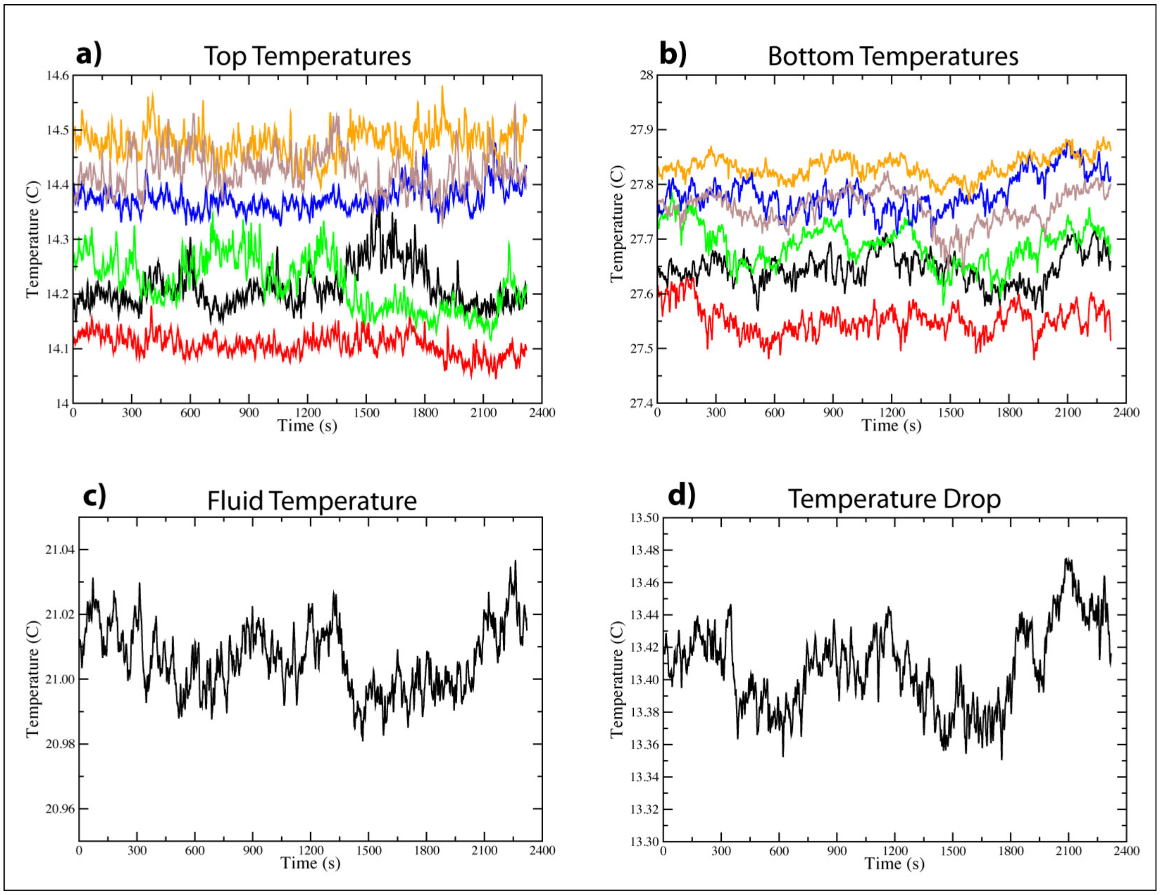

Figure 3. Sample temperature time series measurements from non-rotating convection in a 5 cm tank of water with 100 W heat power applied. **a)** and **b)** are temperature time series measurements from the top and, bottom thermistors, respectively, $T_i^{\mathrm{top}}(t)$ and $T_i^{\mathrm{bottom}}(t)$. **c)**: The thermistor measurements from **a)** and **b)** are averaged to calculate a time series measurement of the mean fluid temperature, $T_{\mathrm{fluid}}(t) = \frac{1}{12}\sum_{i=1}^{6}\left(T_i^{\mathrm{top}}(t) + \sum_{i=1}^{6} T_i^{\mathrm{bottom}}(t)\right)$. **d)**: The difference between mean top and bottom temperatures gives the temperature drop, $\Delta T(t) = \frac{1}{6}\left(\sum_{i=1}^{6} T_i^{\mathrm{bottom}}(t) - \sum_{i=1}^{6} T_i^{\mathrm{top}}(t)\right)$. These measurements are then averaged in time for each convection case, and used to calculate fluid properties and nondimensional parameters.

diffusivity, Ω is angular rotation rate, h is the height of the container, α_T is the fluid's thermal expansivity, g is gravitational acceleration, ΔT is the temperature drop across the convection tank, q is heat flux, and k is the fluid's thermal conductivity. Water is the working fluid for all cases but those with h = 9.8 cm, in which sucrose solution was used.

h (m)	RPM	Power (W)	Pr	E	Ra	Nu
0.032	0	10.82	6.946	∞	1.071×10^{6}	8.189
0.032	0	30.48	6.957	∞	2.352×10^{6}	10.47
0.032	0	50.59	6.989	∞	3.479×10^{6}	11.62
0.032	0	100.4	7.051	∞	5.835×10^{6}	13.44
0.032	0	149.6	6.951	∞	8.237×10^{6}	14.7
0.032	0	199.9	6.459	∞	1.183×10^{7}	16.18
0.032	0	299.5	5.786	∞	1.953×10^{7}	18.44
0.032	4.66	10.85	6.933	9.941×10^{-4}	9.545×10^{5}	9.251
0.032	4.66	50.65	7.098	1.015×10^{-3}	3.026×10^{6}	12.86
0.032	4.66	100.6	6.416	9.284×10^{-4}	6.259×10^{6}	15.61
0.032	4.66	200.2	6.812	9.787×10^{-4}	9.836×10^{6}	17.28
0.032	46.63	10.82	6.767	9.724×10^{-5}	2.703×10^{6}	3.451
0.032	46.63	30.48	6.851	9.83×10^{-5}	4.083×10^{6}	6.253
0.032	46.63	50.6	6.738	9.687×10^{-5}	5.275×10^{6}	8.351
0.032	46.63	100.6	7.081	1.012×10^{-4}	6.842×10^{6}	11.37
0.032	46.63	200.3	6.654	9.581×10^{-5}	1.126×10^{7}	15.94
0.032	46.63	299.9	5.916	8.636×10^{-5}	1.757×10^{7}	19.64
0.0472	0	10.81	6.75	∞	3.843×10^{6}	11.54
0.0472	0	30.47	6.736	∞	8.567×10^{6}	14.67
0.0472	0	50.59	6.84	∞	1.251×10^{7}	16.09
0.0472	0	75.06	6.829	∞	1.704×10^{7}	17.6
0.0472	0	100.3	6.808	∞	2.14×10^{7}	18.85
0.0472	0	200.4	6.349	∞	4.183×10^{7}	22.54
0.0472	0	299.2	5.446	∞	7.318×10^{7}	26.12
0.0472	0	398.9	4.824	∞	1.123×10^{8}	28.2
0.0472	1.91	10.85	6.738	1.087×10^{-3}	3.439×10^{6}	13.01
0.0472	1.91	50.35	6.789	1.094×10^{-3}	1.157×10^{7}	17.63
0.0472	1.91	101.1	6.907	1.111×10^{-3}	1.969×10^{7}	19.96
0.0472	1.91	300.6	5.68	9.348×10^{-4}	6.595×10^{7}	26.88
0.0472	19.1	10.49	6.841	1.102×10^{-4}	4.22×10^{6}	9.895
0.0472	19.1	30.8	6.888	1.108×10^{-4}	7.597×10^{6}	15.87
0.0472	19.1	50.27	6.967	1.12×10^{-4}	1.029×10^{7}	18.6
0.0472	19.1	75.21	6.973	1.12×10^{-4}	1.372×10^{7}	20.84
0.0472	19.1	101	6.98	1.121×10^{-4}	1.709×10^{7}	22.42
0.0472	19.1	200.2	6.823	1.099×10^{-4}	3.043×10^{7}	26.34
0.0472	19.1	300.6	5.873	9.628×10^{-5}	5.46×10^{7}	30.42
0.0472	19.1	400.6	5.173	8.607×10^{-5}	8.416×10^{7}	33.42
0.0472	47.7	10.5	6.806	4.392×10^{-5}	9.41×10^{6}	4.493
0.0472	47.7	30.53	6.782	4.378×10^{-5}	1.443×10^{7}	8.59
0.0472	47.7	50.7	6.833	4.407×10^{-5}	1.786×10^{7}	11.32
0.0472	47.7	75.76	6.84	4.411×10^{-5}	2.159×10^{7}	13.97

continued on next page

h (m)	RPM	Power (W)	Pr	E	Ra	Nu
0.0472	47.7	101.1	6.97	4.485×10^{-5}	2.42×10^{7}	15.9
0.0472	47.7	200.3	6.462	4.195×10^{-5}	3.999×10^{7}	22.67
0.0472	47.7	301.4	5.72	3.767×10^{-5}	6.255×10^{7}	28.03
0.0472	47.7	400.5	5.122	3.417×10^{-5}	8.868×10^{7}	32.28
0.098	0	20.69	10.59	∞	4.329×10^{7}	26.52
0.098	0	50.65	10.03	∞	9.851×10^{7}	32.45
0.098	0	100.4	9.623	∞	1.82×10^{8}	38.19
0.098	0	200.1	8.803	∞	3.599×10^{8}	46.29
0.098	0	299.6	7.518	∞	6.298×10^{8}	52.92
0.098	0	496.4	5.986	∞	1.358×10^{9}	58.32
0.098	0.5	20.69	10.92	1.512×10^{-3}	3.982×10^{7}	26.69
0.098	0.5	50.65	10.86	1.505×10^{-3}	8.197×10^{7}	32.14
0.098	0.5	101	10.6	1.472×10^{-3}	1.517×10^{8}	36.81
0.098	0.5	249.9	8.578	1.211×10^{-3}	4.543×10^{8}	48.16
0.098	5	20.46	10.68	1.483×10^{-4}	3.735×10^{7}	29.72
0.098	5	51.04	10.93	1.514×10^{-4}	7.547×10^{7}	34.61
0.098	5	101.5	10.75	1.491×10^{-4}	1.361×10^{8}	39.87
0.098	5	201.7	9.353	1.312×10^{-4}	3.212×10^{8}	46.2
0.098	5	497.2	6.158	8.953×10^{-5}	1.22×10^{9}	62.37
0.098	25	21.02	10.62	2.949×10^{-5}	4.121×10^{7}	28.07
0.098	25	50.84	11.01	3.049×10^{-5}	6.864×10^{7}	37.17
0.098	25	100.8	10.69	2.966×10^{-5}	1.218×10^{8}	44.87
0.098	25	199.7	9.808	2.74×10^{-5}	2.472×10^{8}	53.64
0.098	25	497.9	6.458	1.87×10^{-5}	1.008×10^{9}	70.34
0.098	50	20.87	10.6	1.472×10^{-5}	6.278×10^{7}	18.38
0.098	50	31.03	10.73	1.488×10^{-5}	7.574×10^{7}	22
0.098	50	50.91	10.64	1.477×10^{-5}	1.006×10^{8}	27.75
0.098	50	75.95	10.86	1.505×10^{-5}	1.214×10^{8}	32.56
0.098	50	100.8	10.87	1.506×10^{-5}	1.425×10^{8}	36.78
0.098	50	150.8	10.45	1.452×10^{-5}	1.97×10^{8}	43.86
0.098	50	201.2	9.655	1.351×10^{-5}	2.751×10^{8}	50.27
0.098	50	251.2	8.971	1.262×10^{-5}	3.625×10^{8}	55.57
0.098	50	301	8.403	1.189×10^{-5}	4.528×10^{8}	60.53
0.098	50	400	7.382	1.056×10^{-5}	6.82×10^{8}	67.29
0.098	50	499.5	6.55	9.469×10^{-6}	9.522×10^{8}	73.04
0.098	50	599	5.855	8.552×10^{-6}	1.281×10^{9}	77.12
0.197	0	10.82	6.852	∞	2.989×10^{8}	43.54
0.197	0	30.73	6.723	∞	6.819×10^{8}	56.64
0.197	0	50.58	6.889	∞	9.764×10^{8}	61.51
0.197	0	100.8	6.816	∞	1.688×10^{9}	72.73
0.197	0	199.8	6.2	∞	3.371×10^{9}	89
0.197	0	299.3	5.474	∞	5.578×10^{9}	103

continued on next page

h (m)	RPM	Power (W)	Pr	E	Ra	Nu
0.197	0	401	4.509	∞	1.099×10^{10}	98.6
0.197	0.123	10.84	6.937	9.943×10^{-4}	2.916×10^{8}	43.41
0.197	0.123	50.67	6.89	9.883×10^{-4}	9.691×10^{8}	62.06
0.197	0.123	101	6.842	9.822×10^{-4}	1.676×10^{9}	72.74
0.197	0.123	200.1	6.336	9.177×10^{-4}	3.26×10^{9}	88
0.197	1.23	10.86	6.898	9.893×10^{-5}	2.771×10^{8}	46.38
0.197	1.23	30.83	6.912	9.911×10^{-5}	6.299×10^{8}	57.66
0.197	1.23	50.78	6.909	9.907×10^{-5}	9.386×10^{8}	63.79
0.197	1.23	101.2	6.873	9.861×10^{-5}	1.623×10^{9}	74.44
0.197	1.23	200.2	6.353	9.2×10^{-5}	3.216×10^{9}	88.73
0.197	3.075	10.84	6.964	3.991×10^{-5}	2.624×10^{8}	47.82
0.197	3.075	30.84	6.947	3.982×10^{-5}	5.938×10^{8}	60.45
0.197	3.075	50.7	6.95	3.984×10^{-5}	8.831×10^{8}	66.74
0.197	3.075	101.1	6.921	3.969×10^{-5}	1.548×10^{9}	76.7
0.197	3.075	200.2	6.416	3.712×10^{-5}	3.054×10^{9}	91.47
0.197	12.3	10.85	6.935	9.938×10^{-6}	2.762×10^{8}	45.9
0.197	12.3	30.83	6.942	9.946×10^{-6}	5.737×10^{8}	62.66
0.197	12.3	50.69	6.967	9.978×10^{-6}	8.353×10^{8}	70.14
0.197	12.3	100.6	6.976	9.99×10^{-6}	1.442×10^{9}	80.37
0.197	12.3	150.6	6.948	9.953×10^{-6}	2.015×10^{9}	86.95
0.197	12.3	201	6.444	9.314×10^{-6}	2.936×10^{9}	94.63
0.197	12.3	299.9	5.509	8.109×10^{-6}	5.221×10^{9}	109
0.197	41.01	10.33	6.84	2.945×10^{-6}	6.037×10^{8}	20.66
0.197	41.01	14.94	6.823	2.939×10^{-6}	7.139×10^{8}	25.41
0.197	41.01	19.96	6.819	2.937×10^{-6}	8.006×10^{8}	30.32
0.197	41.01	24.7	6.91	2.972×10^{-6}	8.634×10^{8}	33.73
0.197	41.01	29.94	6.992	3.003×10^{-6}	9.316×10^{8}	36.83
0.197	41.01	40.09	7.012	3.01×10^{-6}	1.06×10^{9}	43.04
0.197	41.01	50.04	7.037	3.02×10^{-6}	1.178×10^{9}	47.91
0.197	41.01	74.76	7.009	3.009×10^{-6}	1.481×10^{9}	57.49
0.197	41.01	101.2	6.991	3.002×10^{-6}	1.783×10^{9}	65.08
0.197	41.01	150.6	6.814	2.935×10^{-6}	2.436×10^{9}	75.31
0.197	41.01	201	6.418	2.784×10^{-6}	3.017×10^{9}	92.88
0.197	41.01	192.2	6.242	2.717×10^{-6}	3.496×10^{9}	81.33
0.197	41.01	299.8	5.451	2.41×10^{-6}	5.515×10^{9}	105.2
0.197	41.01	284.9	5.297	2.35×10^{-6}	6.422×10^{9}	90.52
0.197	41.01	400.2	4.539	2.051×10^{-6}	1.063×10^{10}	100.6

REFERENCES

Hirst, W & Cox, R 1976 The construction and analysis of sucrose gradients for use with zonal rotors. *Biochemical Journal* **159**, 259–265.

Johnston, H & Doering, C 2009 Comparison of turbulent thermal convection between conditions of constant temperature and constant flux. *Physical Review Letters* **102**, 064501–4.

King, E, Stellmach, S, Noir, J, Hansen, U & Aurnou, J 2009 Boundary layer control of rotating convection systems. *Nature* **457** (7227), 301–304.

King, E M 2009 An investigation of planetary convection: The role of boundary layers. PhD thesis, University of California, Los Angeles.

Lide, David R. 2000 *Handbook of Chemistry and Physics*. CRC Press.

Lopez, J & Marques, F 2009 Centrifugal effects in rotating convection: nonlinear dynamics. *Journal of Fluid Mechanics* **628**, 269–297.

Verzicco, R 2004 Effects of nonperfect thermal sources in turbulent thermal convection. *Physics of Fluids* **16** (6), 1965–1979.

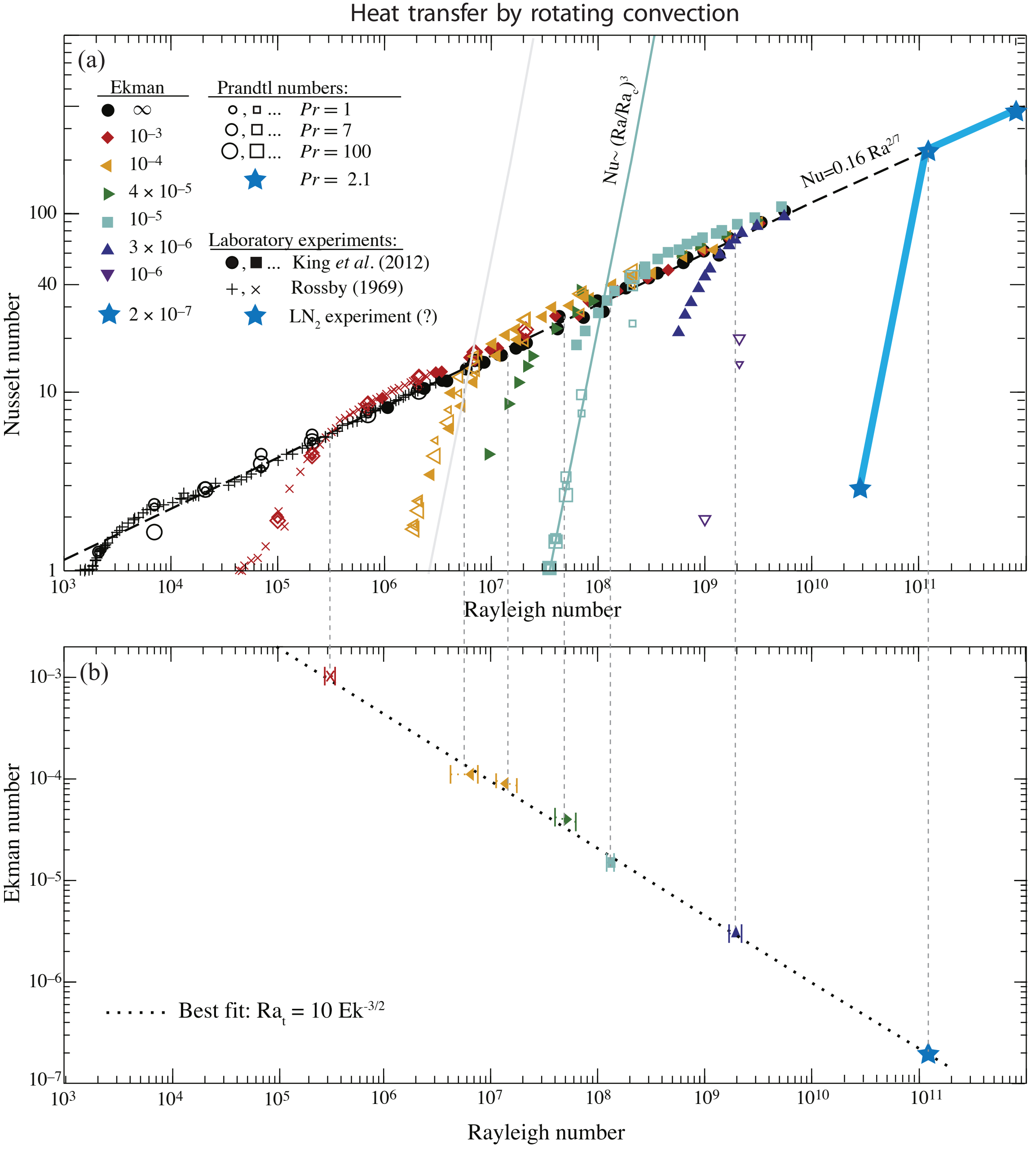
Heat transfer by rotating convection